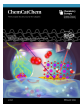

Manganese Oxide as an Inorganic Catalyst for the Oxygen Evolution Reaction Studied by X-Ray Photoelectron and Operando Raman Spectroscopy

Hannes Radinger,*[a, b] Paula Connor,[a] Robert Stark,[c] Wolfram Jaegermann,[a] and Bernhard Kaiser*[a]

Manganese oxide (MnO_x) is considered a promising material for the oxygen evolution reaction (OER) to replace noble metal catalysts in water splitting. The improvement of MnO_x requires mechanistic and kinetic knowledge of the four-electron transfer steps of the OER. X-ray photoelectron spectroscopy, a widely used tool to characterize the electronic structure of thin films, is used in combination with surface-enhanced Raman spectroscopy to gain a deeper knowledge of the different mixed MnO_x types and their respective change in chemical composition. Using Raman spectroscopy during electrochemical measurements, all samples were found to reveal Birnessite-type MnO_2 motifs in alkaline media at an applied potential. Their activity correlates with two shifting Raman active modes, one of them being assigned to the formation of Mn^{III} species, and one to the expansion of layers of MnO_6 octahedra. A special activation treatment leads independent of the starting material to a highly amorphous mixed-valence oxide, which shows the highest OER activity.

1. Introduction

Today the global energy utilization mostly depends on fossil fuels, but energy supplies are expected to run out within the next 150 years.[1] Furthermore, the increasing emission of the greenhouse gas CO_2 leads to global warming with serious consequences. Therefore, a rising interest in the exploration of solar fuels is observed as an environmentally friendly and abundant replacement for fossil fuels.[2,3] Renewable energies from wind and sun show a fluctuating availability over time.[4,5] Therefore, an effective high energy chemical, such as molecular hydrogen, to store large amounts of energy is required.[6] Hydrogen is the most abundant element in the universe; it possesses two to three times the specific energy density of gasoline, and it is carbon-free as a plus.[7,8] The production of hydrogen *via* electrolysis requires two half-cell reactions, namely the hydrogen evolution reaction (HER: $2H^+ + 2e^- \rightarrow H_2$) and the oxygen evolution reaction (OER: $2H_2O \rightarrow O_2 + 4H^+ + 4e^-$), in which the latter is seen as the bottleneck of water splitting as a result of its sluggish kinetics and the high overpotential required.[9,10] A promising material class to replace the benchmark noble metal catalysts for the OER are transition metal oxides, manganese oxides (MnO_x) as prototypical oxide is not only occurring in nature as water oxidizing catalyst Photosystem II (PS II), but it is also earth-abundant, cheap, durable, and non-toxic.[11–14] MnO_x exists in a variety of crystal structures and valences ranging from +II to +VII. $Mn^{II}O$ has a rock salt structure with Mn^{II} cations and octahedrally coordinated O^{2-} anions, whereas Mn_2O_3 forms α-Mn_2O_3 with cubic bixbyite structure above 500 °C.[15–17] At least six polymorphs of MnO_2 have been characterized, *e.g.* the tunnel structured α-MnO_2 or the layered δ-MnO_2which differ in their degree of crystallinity and their chemical composition.[18–21] All MnO_2 structures are classified by a network of oxygen atoms with Mn^{IV} cations forming MnO_6 octahedra. These octahedra are distorted and therefore have different number, chain length, and Mn–O distances.[19,22]

The desire to rationally design OER catalysts gives rise to the exploration of *in situ/operando* characterization techniques to understand active sites and reaction pathways.[23–25] Raman spectroscopy is particularly convenient for *operando* spectroscopy, since it uses visible light, gives strong signals for typical catalytically active sites, such as molecular metal oxide vibrations, and it is applicable under electrochemical conditions in aqueous solutions.[26,27] A working spectro-electrochemical setup allows for the simultaneous characterization of activity and selectivity.[28] For instance, by *operando* Raman spectroscopy, MnO_x samples were found to be oxidized to MnO_2 in $Na_2B_4O_7$ during cycling, and metallic manganese transforms to

[a] H. Radinger, Dr. P. Connor, Prof. W. Jaegermann, Priv.-Doz. Dr. B. Kaiser
Surface Science Laboratory
Institute of Materials Science
TU Darmstadt
64287 Darmstadt (Germany)
E-mail: kaiser@surface.tu-darmstadt.de
[b] H. Radinger
Institute for Applied Materials
Karlsruhe Institute of Technology
76344 Eggenstein-Leopoldshafen (Germany)
E-mail: hannes.radinger@kit.edu
[c] Prof. R. Stark
Physics of Surfaces
Institute of Materials Science
TU Darmstadt
64287 Darmstadt (Germany)

Supporting information for this article is available on the WWW under https://doi.org/10.1002/cctc.202001756

MnO_2 above 1.4 V *vs.* RHE in alkaline media.[29,30] A further study assigned vibrational bands observed at a negative potential applied to metallic manganese in alkaline media to hollandite-like α–MnO_2.[31] Thin films of electrodeposited MnO_2 have also been studied at cathodic potentials before and revealed the reversible formation of MnOOH and $Mn(OH)_2$.[32] Since the catalytic activity is mainly dependent on the surface of the metal oxide, studying thin films ($\leq$10 nm) of material is mandatory. To observe chemical changes under working conditions, surface-enhanced Raman scattering (SERS) is performed to increase the inelastic scattering of light and therefore the Raman signal.[33]

Reviewing the available literature on electrocatalytic performance shows that the behavior of MnO_x as a function of applied voltage depends on a variety of factors, such as the oxidation state, crystal structure, electrolytic environment, and synthesis method. X-ray Photoelectron spectroscopy (XPS) has been established in catalysis as a powerful tool to investigate the composition and electronic structure of a solid surface.[34] It allows one to quantify the oxidation states of a material such as multivalent manganese oxides.[35] In most cases, the surface of a catalyst is studied before and after a reaction took place. It is helpful to combine all analytical tools available and the information each one provides to fully understand the catalytic processes.[36]

In this work, thin films of MnO_x ($Mn^{II}O$, $Mn^{III}{}_2O_3$, $Mn^{IV}O_2$) produced by reactive magnetron sputtering, deposited on electrochemically roughened gold substrates, have been characterized and investigated as electrocatalysts for oxygen evolution in alkaline media. On-line vacuum coupled XPS has been used to identify the initial electronic structure of MnO_x and the corresponding alteration after electrochemical cycling. Surface-enhanced *operando* Raman spectroscopy was employed before, after, and during electrolysis to study the structural composition and changes of the amorphous, mixed MnO_x at all states. Based on the observations in these studies, using a combination of electrochemical activation and reduction, and investigation of the modification by XPS and SERS, the catalytic activity of MnO_x has been enhanced, but still does not show high performance as compared to Ni or Co-based oxides.

Experimental

Substrate Preparation: Coin-shaped gold plates (Schiefer & Co., 99.9% purity) with a diameter of 12 mm have been used as substrate. These have been polished to mirror finish with 0.05 μm Alumina MicroPolish (Buehler), and surface-enhanced by an etching process, using 0.1 M KCl, described in detail by Diaz-Morales *et al.*[37] The roughness was investigated by atomic force microscopy (AFM), leading to the conclusion that the etching process is capable of multiplying the average roughness by a factor of 4.2 by creating a homogeneous structure with islands of 350–450 nm in diameter (see Figure S1). The effect of the surface enhancement has been investigated by comparing the Raman signal of a thin MnO_2 film on a polished and roughened gold substrate (Figure S2).

Sample Deposition: MnO_x has been deposited by reactive magnetron sputtering at room temperature using a metallic manganese target (Kurt J. Lesker, 99%) and a gas mixture of argon (Air Liquide, 99.999%) and oxygen (Air Liquide, 99.995%). The amount of gas flow was regulated with mass flow controllers (MKS Instruments) to control the stoichiometry of the samples. The deposition was carried out at a DC sputter power of 20 W at a total pressure of 0.03 mbar, varying the gas flow from 19.6–19.9 sccm argon and 0.1–0.4 sccm oxygen to prepare the Mn^{II} and Mn^{IV} samples. Mn^{III} was produced by annealing Mn^{IV} for 1 h at 600 °C under a 20 sccm argon gas flow.

X-Ray Photoelectron Spectroscopy: The chemical composition was investigated by XPS (Specs Phoibos 150, Focus 500 with XR50 M) in line at pressures of 5×10^{-10} mbar or below. As an X-ray excitation source, a monochromatized AlK_α line at 1486.74 eV was used. Survey spectra were recorded with a pass energy of 25 eV, which was reduced to 10 eV for detail spectra. The spectra were evaluated with the software CasaXPS to employ a Shirley background correction, and Gaussian-Lorentzian peak functions to derive specific components in deconvolution, adjusting the peak intensity and the full width at half maximum (FWHM).

Electrochemistry: Half-cell measurements were performed in an electrochemical cell (Zahner PECC-2), using 0.1 M KOH (Carl Roth, 99.98%) as the electrolyte in a three-electrode setup. An Ag/AgCl or Hg/HgO electrode was calibrated against a reversible hydrogen electrode (RHE, HydroFlex, Gaskatel) in the electrolyte before the experiments and used as reference thereafter. A platinum wire served as a counter, and the sample as a working electrode, connecting the setup to a potentiostat (Gamry 1000). The potential was *iR*-corrected by electrochemical impedance spectroscopy (EIS) at the respective open circuit potential (OCP), which is exemplary displayed in Figure S3. After 10 min, the OCP ($<$100 mV) of the system was determined and the impedance measured at this potential with an alternating voltage of $\pm$10 mV in a frequency range of 1 MHz to 5 Hz.

Raman Spectroscopy: Raman spectra were recorded using a micro-Raman spectrometer (Horiba HR800), equipped with a HeNe laser (632.8 nm). The plasma emission was filtered with an interference filter, and a Raman notch filter has been used for laser light rejection. The measurements were performed with a grating of 600 grooves mm^{-1}, and a 100× microscope (NA 0.8) for dry samples, whereas *operando* measurements were carried out with a 50× microscope (NA 0.55). For *operando* spectroscopy, an *in-situ* cell (rhd instruments, TSC Raman cell) has been used, allowing irradiation of the sample through a transparent SiO_2 window. An Ag/AgCl micro-reference electrode was calibrated against RHE and installed in the cell to control the potential with a Gamry 1000 potentiostat. Inside the cell, a gold-plated ring served as the counter electrode. The sample is placed on a PEEK encased copper cylinder as the working electrode. All spectra were taken setting the Raman microscope pinhole size to 950 μm and the slit size to 50 μm. The laser power was attenuated using neutral density (ND) filters, employing 0.01–0.5 mW irradiation at a spot size of 0.8–1.4 μm to avoid structural changes. Especially Mn_2O_3 is easily reduced under laser irradiation but was found stable at 1 mW of 632.8 nm laser light before.[38] Prior to the recording of *operando* spectra, the samples were conditioned inside the *in-situ* cell between 1.0–1.5 V *vs.* RHE by cycling 50 times with 100 mV s^{-1}. A potential of 1.0 V *vs.* RHE has been applied afterward for at least 10 min to stabilize surface processes. The discussed spectra are the average of 20 scans with 3–5 s irradiation time. All Raman spectra were normalized to the highest peak without background correction.

2. Results and Discussion

2.1. Characterization: XPS

At the start of every XPS investigation, a survey measurement (Figure S4) of each sample was performed to exclude surface contamination. As the samples were prepared in an ultra-high vacuum (UHV) system (10^{-8}–10^{-10} mbar base pressure) and the spectra were recorded in line (transfer from preparation to analysis without breaking the vacuum), no carbon-containing impurities were detected on the surface. The most intense gold core level region Au 4f (lit.: 84–88 eV) of the substrate overlaps with the manganese Mn 3s core level peak (lit.: 83–89 eV, see Figure S2).[39,40] For all experiments, the Mn 2p, O 1s, C 1s (to check for contamination), Mn 3s, and Mn 3p core-level regions were recorded along with the secondary electron and valence band edge.

A common approach to determine the oxidation state of MnO_x is the evaluation of the peak binding energy distance in the multiplet split Mn 3s region or the binding energy distance $\triangle E2p_{1/2}$ between the Mn $2p_{1/2}$ peak and its satellite.[41,42] Additional information regarding the oxide phases is delivered by the O 1s region. It is not possible to exclude any influence of the weak Au $4p_{1/2}$ (lit.: ~643 eV) core level peak on the Mn 2p region, leaving only the Mn 3p region for stoichiometric evaluation.[39] As a result of the strong overlap of the Mn 3s and the Au 4f region (Figure S5) a well-defined evaluation of the Mn 3s multiplet distance is excluded, and only the Mn 2p region is used to identify the main oxidation state of the freshly prepared thin film. Therein, the position of the $2p_{1/2}$ peak and the $2p_{1/2}$ satellite and consequently the distance $\Delta E2p_{1/2}$ is determined. The XP detail spectra of this region are displayed in Figure 1(a) and the determined peak locations and distances $\Delta E2p_{1/2}$ are summarized in Table 1. Based on the comparison with literature data, MnO_x has been synthesized in three different main oxidation states, as MnO (Mn^{II}), Mn_2O_3 (Mn^{III}), and MnO_2 (Mn^{IV}).[31,43] The O 1s region (Figure 1(b–d)) was deconvoluted by Gaussian-Lorentzian peak shapes to analyze the different oxygen-containing components. The lattice oxygen (O_L) is present at binding energies of 529.6–530.4 eV with FWHM values of 0.9–1.1 eV, and is therefore at slightly higher binding energies than it has been reported in the literature (up to 530.0 eV), probably due to under stoichiometric deposition, further indicated by the metallic manganese shoulder at ~639 eV for the Mn^{II}-phase.[40,44,45] Mn^{III} and Mn^{IV} contain additional oxides in oxidation states different from the main phase, which are assigned based on the position of the O_L peak of the respective main phase. All three samples further reveal vacancy induced oxygen components (O_V) at a binding energy of 531.0–532.1 eV with higher FWHM values of 1.4–1.7 eV.[46,47] The higher FWHM of 1.7 eV in Mn^{III} and Mn^{IV} is the result of defect states induced by three different O_L components, whereas Mn^{II} contains only one defective component. From the fits, one can observe that the defect density decreases from the Mn^{II} compound (~18.5%) to the Mn^{IV} compound (~5.7%). The stoichiometry was evaluated using all three O_L components and the area of the Mn 3p region (Figure S5). Mn^{II} and Mn^{III} are over-stoichiometric with Mn/O ratios of 1.11 (ideal: 1.00) and 0.73 (ideal: 0.66), while Mn^{IV} contains excessive oxygen at a ratio of 0.44 (ideal: 0.50) and is therefore under-stoichiometric. These deviations can be attributed to the partial deposition of metallic manganese on Mn^{II}, and the synthesis of mixed MnO_x phases.

Table 1. X-Ray photoelectron spectroscopy determined values for spin orbital splitting Mn $\Delta E2p_{1/2}$ of freshly deposited MnO_x.[31,42]

Sample	$2p_{1/2}$ [eV]	Sat. ($2p_{1/2}$) [eV]	$\Delta E2p_{1/2}$ [eV]	Lit. [eV]
Mn^{II}	653.4	659.3	5.9	5.4–6.0
Mn^{III}	653.0	663.1	10.1	10.0–10.5
Mn^{IV}	653.3	664.8	11.8	11.8–11.9

2.2. Characterization: Raman Spectroscopy

While XPS is usually a powerful tool to investigate the chemical composition of amorphous thin films, the interpretation of XPS data is difficult in the case of MnO_x due to the sheer number of structures, morphologies, and shapes that exist for each corresponding oxidation state.[48–50] To understand the efficiency towards water splitting, it is especially important for mixed manganese oxides to probe the exact chemical composition because the mix can contain up to three different manganese valences in various concentrations.[35,51] Another obstacle is the difference in signal intensity of different MnO_x species. This does not only vary between the oxidation state of manganese, or based on the structural type, but also within a structure such as Birnessite.[19,22] The Raman band position and shape therein depends on the shared edges between MnO_6 octahedra or the average Mn–O distance. Since the XPS results revealed that our samples consist of a mixture of different oxides, a quantitative approach to this problem cannot be expected by the Raman results. To this end, surface-enhanced Raman spectra (SERS) were recorded on the freshly deposited samples (within 10 min after atmospheric contact) to gain a better understanding of the short-range order, the arrangement of MnO_x clusters, and the phase mixture. To avoid heat-induced structural changes, the samples were illuminated using the highest available neutral density (ND) filter, to reduce the power of the laser beam to around 0.1 mW at a spot size of ~800 nm. This value is well below the laser power employed in recent investigations for the decomposition of different manganese oxide compounds.[52,53] Nevertheless, laser-induced degradation cannot be completely excluded.[54]

A MnO_x Raman spectrum is generally characterized by two distinct marker modes between 450–550 cm^{-1} and 550–750 cm^{-1}.[19,55] These relatively intense peaks describe the Mn–O vibrations as distortion modes of Mn–O–Mn chains parallel (in-plane), and stretching modes of Mn–O perpendicular (out-of-plane) to the basal plane, often denoted as $A_g(1)$ and $A_g(2)$.[56] The wavenumber of these modes is associated with the polymerization degree of MnO_6 octahedra and the interlayer spacing between layers of MnO_6.[19,22,57] One has to be aware of the discrepancies in the literature regarding the collected

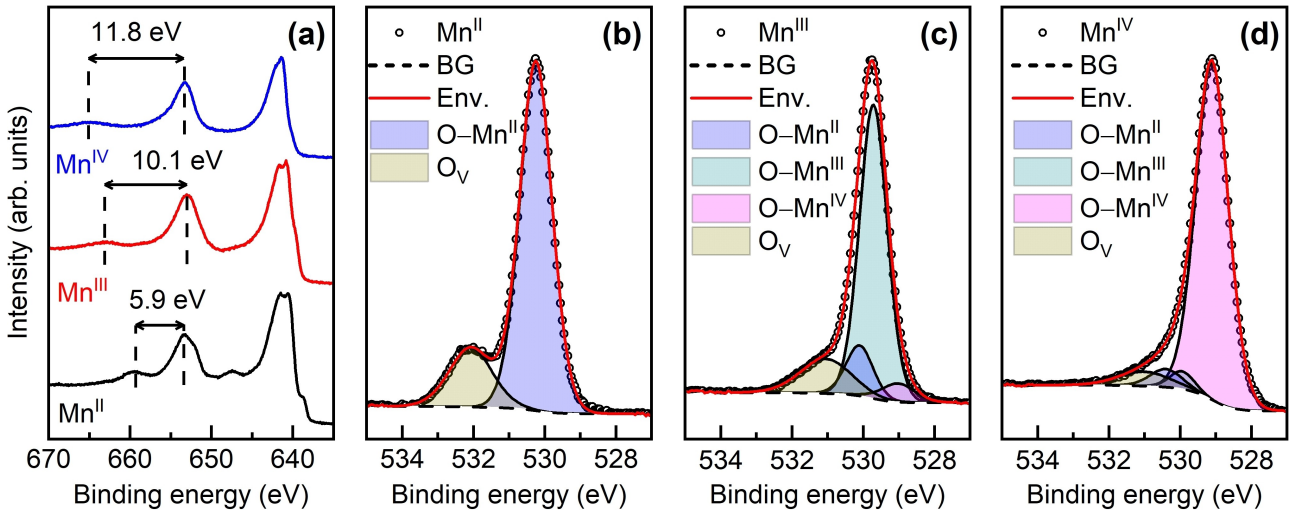

Figure 1. X-Ray photoelectron detail spectra of as deposited MnO_x. In the manganese core level region Mn 2p (a), the binding energy distance of the $2p_{1/2}$ peak and the $2p_{1/2}$ satellite is indicated. The O 1s region displays the different lattice (O_L) and vacant (O_V) oxygen components of Mn^{II} (b), Mn^{III} (c), and Mn^{IV} (d), deconvoluted by Gaussian-Lorentzian peak shapes.

spectra of natural and synthetic MnO_x, and keep in mind differences as a result of synthesis routes, used techniques to identify the main phase, experimental conditions such as laser power or light irradiation time, and the wide variety of phase mixtures.[29,53–55,58] It should be noted here, that the SERS technique itself might have a strong influence on relative peak intensities and positions because of the involved redistribution of electron density and charge-transfer effects.[59,60] From the XPS data of Mn^{II}, we would expect a Raman scattering spectrum, which closely resembles that of Manganosite (MnO) showing a characteristic peak at around 530 cm^{-1}.[19,55] This is not the case, instead we observe a strong peak at 568 cm^{-1} (Figure 2(a)), which has been attributed previously to the stretching mode of divalent manganese cations.[19] The other visible strong and weak peaks at 660, 600, 465, and 323 cm^{-1} are most probably due to fast oxidation of the MnO to Mn_2O_3 (Bixbyite) or Mn_3O_4 (Hausmannite) under atmospheric conditions or to a laser-induced decomposition of the starting material MnO.[19,55,61,62] In XPS a minor amount of metallic

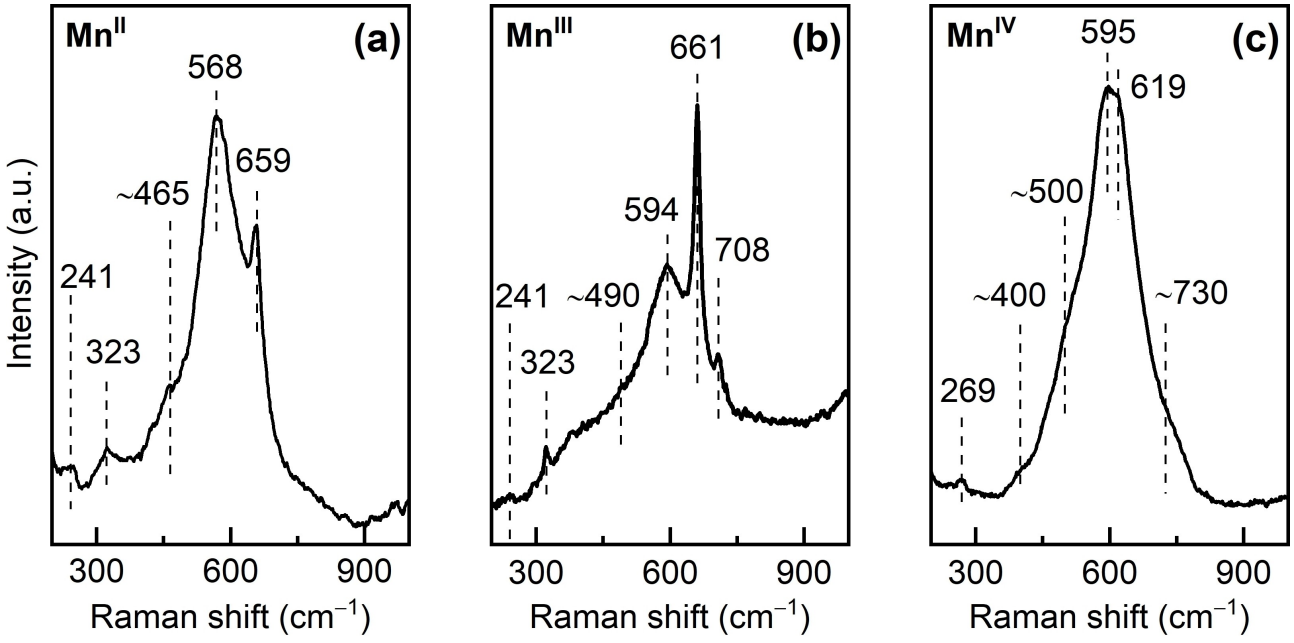

Figure 2. Surface enhanced Raman spectra of as prepared manganese oxides (a) Mn^{II}, (b) Mn^{III}, and (c) Mn^{IV}. The wavenumber of the observed vibrational features is indicated.

manganese has been observed, which is probably either oxidized under irradiation or decomposes as well.

The Raman spectrum of Mn^{III} in Figure 2(b) reveals a striking three-band profile at 594, 661, and 708 cm^{-1} (lit.: 592, 645, and 698 cm^{-1}), characteristic for α-Mn_2O_3 (Bixbyite).[19] Based on the overall shape and intensity of the 661 cm^{-1} peak, a strong contribution of Mn_3O_4 (Hausmannite) is most probable, which also correlates to the difference in stoichiometry observed in XPS. Since the Mn^{III} phase has been prepared by thermal decomposition at 600 °C of the Mn^{IV} phase, the formation of a mixture of Mn_2O_3 and Mn_3O_4 is to be expected, which is indeed observed.

For Mn^{IV}, at least six phase modifications are possible to form a solid film.[61] The Raman scattering spectrum in Figure 2(c) shows a broad signal with a maximum at about 595 cm^{-1}. The deconvoluted spectrum is given in Figure S6. Shoulders can be observed at about 400, 500, 619, and 730 cm^{-1}. From the overall shape, the spectrum resembles that of the Todorokite and Cryptomelane phases, but there is a strong discrepancy between the maximum position of the scattering peak. Whereas we observe the maximum at about 600 cm^{-1}, from the literature data of Todorokite and Cryptomelane a maximum at about 630 cm^{-1} is expected. Additionally, these compounds do not show any clear signals below 500 cm^{-1}.[55] Therefore, we conclude, that we observe here a mixture of a manganese dioxide as the main phase with a lesser amount of lower valent manganese(III)oxides, most likely Bixbyite (α–Mn_2O_3), which leads to the very broad Raman signal. This interpretation correlates also well with the oxidation state derived from our XPS measurements. The vibrational modes observed in Figure 2(c) at about 500, 595, and up to 620 cm^{-1} are characteristic for manganese dioxides and based on their location and shape are either attributed to Birnessite or to Hollandite as the main phase (500, 570–590, 630–650 cm^{-1}).[55,63] Hollandite is a tunnel structured manganese dioxide, formed by double chains of $Mn^{III,IV}O_6$ octahedra.[64] The tunnels can incorporate large cations, such as Ba^{2+} in its mineral form, or water molecules.[55] Birnessite is one of the few manganese dioxides with Raman scattering modes above 700 cm^{-1}, which correlates with the observed band at around 730 cm^{-1}.[19] In the lower wavenumber region below 400 cm^{-1}, Hollandite shows no visible features while in our work there is a peak located at 269 cm^{-1} along with a broader feature at around 400 cm^{-1}, which would support the assignment of a Birnessite-type phase as the main dioxide component.[55] The Birnessite group consists of MnO_6 octahedral layers with a vacancy in every sixth octahedral site, containing hydrated Mn^{III} cations. These manganese-containing layers in the mineral form are separated by layers of lower-valent cations or by layers of water.[22] It has been shown that in Raman spectroscopy band shifts are correlated with the Mn–O bond order and length in the MnO_6 octahedra.[22,65] The 595 cm^{-1} peak corresponds to the in-plane stretching vibration, and the two modes at 500 and 619 cm^{-1} to the out-of-plane vibration of the MnO_6 octahedra.[56,63] The three vibrational marker modes are not at fixed positions but differ based on the number of vacancies in the MnO_6 layer. For instance, the out-of-plane mode above 600 cm^{-1} is known to exhibit a blue-shift with an increased number of Mn^{III} species.[22,56] Overall, these data support our compositional assignment and explain the observed peak maximum at 595 cm^{-1} as well as the shoulders at 500 and 619 cm^{-1}.

In summary, the overall shape of the Raman spectra matches the XPS results about the suspected main oxidation state of the sputter-deposited thin film. With our thin-film system of <10 nm XPS and Raman spectroscopy are sensitive for the whole sample thickness, and the data from both techniques can be correlated easily. With both techniques, we detected a mixture of different manganese oxides. This was quantified with XPS, but the Raman results do not further elaborate on these observations, since too many distracting effects are introduced by the surface enhancement, and due to the overall sensitivity of different MnO_x phases and structures. However, the advantages of Raman spectroscopy are numerous. While XPS is used to determine the electronic structure, the short-range order (especially of amorphous thin films, where X-Ray diffraction cannot be applied) can only be investigated by an additional technique. In the case of MnOx, a lot of information was obtained about the structural type and its degree of crystallinity.

2.3. Electrochemistry

The catalytic performance of the MnO_x thin films produced by reactive magnetron sputtering was investigated by cyclic voltammetry (CV) in 0.1 M KOH electrolyte, applying scan rates of 10 and 50 mV s^{-1}. The surface of the freshly prepared samples was conditioned prior to the experiment by cycling 50 times with 100 mV s^{-1} between 1.0–1.5 V *vs.* RHE. The CV curves to investigate the oxygen evolution characteristics were recorded up to 1.8 V *vs.* RHE (Figure 3). The inset plot shows a more detailed view of the pre OER segment. Mn^{III} has no oxidative

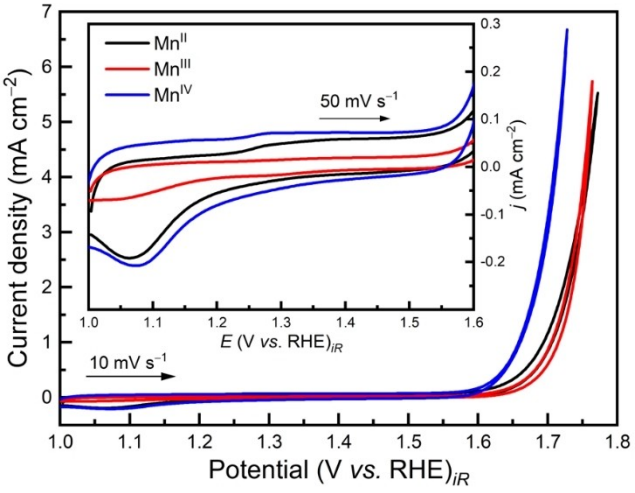

Figure 3. Cyclic voltammetry curves of magnetron sputtered MnO_x in 0.1 M KOH. The inset plot displays the redox waves, which were recorded with a higher scan rate.

current response before the oxygen evolution starts, and only a weak reduction signal up to a current density of $-0.07\ mA\,cm^{-2}$. Mn^{II} and Mn^{IV} oxidative processes are visible at around 1.25 V *vs.* RHE, along with stronger reduction current densities of approximately $-0.2\ mA\,cm^{-2}$ at 1.07 V *vs.* RHE. According to the Pourbaix diagram, in this potential range, the Mn^{IV}/Mn^{III} conversion is expected.[66] A potential dependent change of the redox state in this region has also been observed by X-Ray absorption studies.[67] The redox wave is only weakly pronounced for Mn^{III}, which indicates a low manganese oxide conversion of the material. Table S1 summarizes the kinetic parameters of all measured samples. Mn^{IV} reveals the lowest onset potential (1.60 V *vs.* RHE), lowest overpotential at a current density of $5\ mA\,cm^{-2}$ (490 mV), and lowest Tafel slope ($62\ mV\,dec^{-1}$). Whereas Mn^{III} has the highest OER onset potential (1.64 V *vs.* RHE), the lower Tafel slope of $77\ mV\,dec^{-1}$ compared to Mn^{II} results in a lower overpotential (540 mV) at higher current densities. The reactively sputtered MnO_x catalysts not only differ in their surface properties, *i.e.* their electrochemical available surface area and charge transport, but also in their intrinsic activity due to the difference in the Tafel slopes.[68,69]

2.4. *Operando* Raman Spectroscopy

All three MnO_x samples have been studied under working conditions in 0.1 M KOH at anodic potentials to investigate the reaction mechanism and their differences concerning the synthesized oxidation state and structure. Figure 4 displays the normalized SER spectra stacked with increasing applied potential to illustrate the observed bands and their respective shifts. Prior to the experiments, a Raman spectrum at the open circuit potential (OCP) was recorded before cycling the samples 50 times from 1–1.5 V *vs.* RHE with $100\ mV\,s^{-1}$ for surface conditioning.

At the OCP, Mn^{II} in Figure 4(a) exhibits a small $A_g(1)$ peak at $587\ cm^{-1}$ and an additional small feature at approximately $660\ cm^{-1}$, revealing a similar structure as the freshly prepared sample. The weak mode at $587\ cm^{-1}$ increases significantly and a small feature arises at around $500\ cm^{-1}$ at an applied potential of 0.8 V *vs.* RHE. At 1.1 V *vs.* RHE, an intense $A_g(2)$ mode is identified at $614\ cm^{-1}$, blue-shifting towards $627\ cm^{-1}$ as the potential increases, indicating the introduction of catalytically active Mn^{III} species.[56,63] While this feature is most prominent at 1.35 V *vs.* RHE, a decrease in relative intensity can be observed at higher potentials. At an applied potential of 1.7 V, the previously identified Mn^{II} reveals the characteristic three-band profile of a $Mn^{III,IV}O_x$-type manganese oxide. At approximately $875\ cm^{-1}$ a weak signal is observed, which is most likely due to the formation of MnO_4^-, and it is assumed to originate from K^+ ions situated to a Mn–O bond perpendicular to the lattice plane.[70–72]

Mn^{III} has a very low Raman intensity at the OCP (Figure 4(b)) and shows a broad signal with no very clear specific features. While characteristic Mn^{III} features are still present, the formation of $Mn^{IV}O_2$ can be suspected. This is supported by a rising peak below $500\ cm^{-1}$, which is located at $494\ cm^{-1}$ at applied potentials from 0.8 to 1.7 V *vs.* RHE. From 1.1 to 1.7 V *vs.* RHE, the $A_g(1)$ mode is fixed at $594\ cm^{-1}$. At 1.0 V *vs.* RHE the $A_g(2)$ mode arises at $614\ cm^{-1}$ prominently up to 1.45 V *vs.* RHE. At the same potential, a new shoulder occurs at $658\ cm^{-1}$. Unlike Mn^{II}, no shift of the $A_g(2)$ mode is observed. The *operando* spectrum of Mn^{III} looks almost identical to that of the Mn^{II} at a potential of 1.7 V *vs.* RHE.

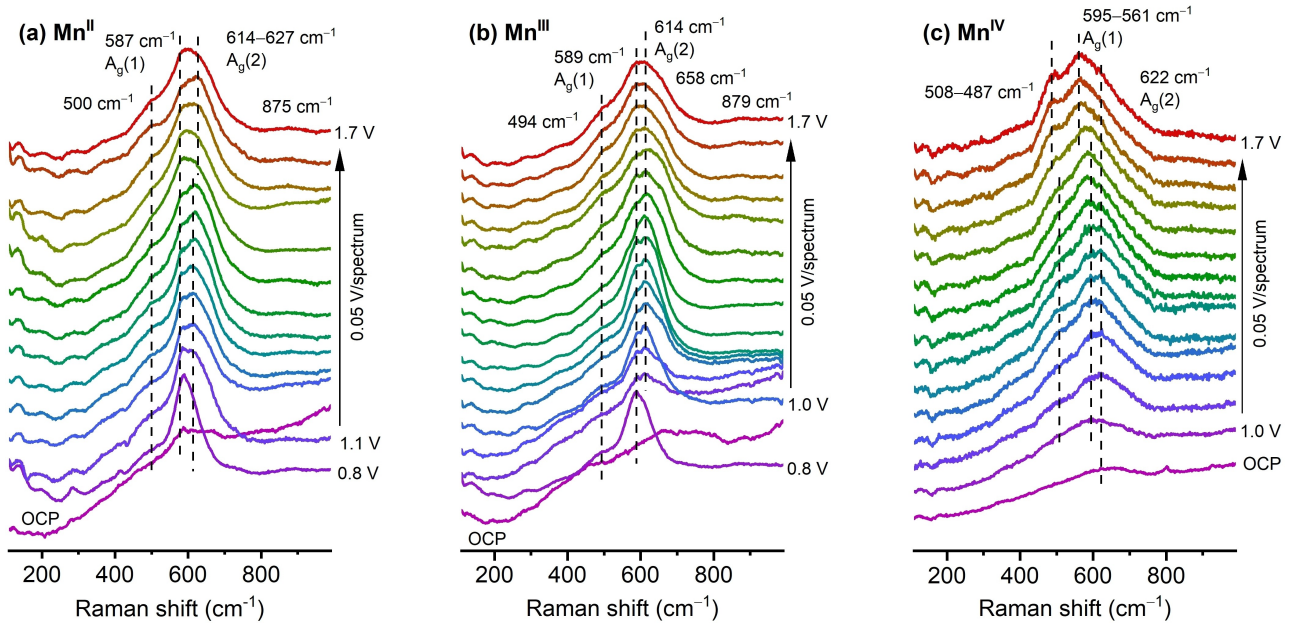

Figure 4. *Operando* surface enhanced Raman spectra of (a) Mn^{II}, (b) Mn^{III}, and (c) Mn^{IV}. Graphs are stacked as the potential increases from bottom to top. The most prominent modes and mode shifts, respectively, are indicated.

At OCP, Mn^{IV} in Figure 4(c) shows only a very broad signal, which cannot be assigned easily. With increasing potential, one broad band appears at 599 cm^{-1}. This is due to the rising $A_g(1)$ mode, located at 595 cm^{-1} at 1.1 V, red-shifting to 561 cm^{-1} as the potential is increased up to 1.7 V *vs.* RHE. The $A_g(2)$ mode in Mn^{IV} is located at 622 cm^{-1}, arising visibly at around 1.25 V *vs.* RHE, and staying constant thereafter up to 1.7 V *vs.* RHE. A broad feature at around 508 cm^{-1} is slowly becoming more prominent with increasing potential, showing a distinct peak at 487 cm^{-1} at higher potentials.[56] Whereas this vibration is present at ~500 cm^{-1} for our Mn^{IV} sample, a lower Raman shift has been observed for Hausmannite ($Mn^{II,III}$) or Manganosite (Mn^{III}), and also our lower valent MnO_x samples.[55] This observation, along with the blue-shifted $A_g(2)$ mode, highly suggests the formation of Mn^{III} species at applied potentials. The overall signal shape and potential-dependent change resembles that of recent *operando* Raman measurements of mixed Bixbiyte/Birnessite phases.[56] This supports our interpretation, that our synthesis process has initially formed a mixture of Mn^{III} and Mn^{IV} containing compounds.

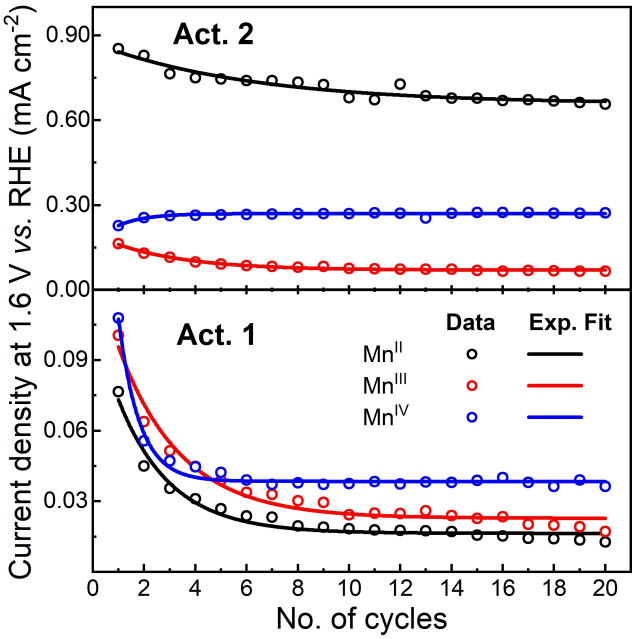

Figure 6. Current density at 1.6 V *vs.* RHE of MnO_x during both activation treatments as a function of conducted cycle.

2.5. Improving MnO_x activity

All samples were electrochemically activated by cycling 20 times in a potential range of 1.2–1.7 V *vs.* RHE with a scan rate of 5 mV s^{-1} (Act_1). As opposed to the previous, fast cycling surface conditioning treatment, the potential is increased up to a value, at which oxygen evolution occurs, and phase transitions as an introduction of Mn^{III} species have been observed in *operando* Raman spectroscopy. Afterwards, a potential of 0.8 V *vs.* RHE was hold for 30 min in a chronoamperometry step, before repeating the described activation treatment (Act_2). The activity of the samples was then investigated by linear sweep voltammetry (LSV) at 1.0–1.9 V *vs.* RHE with a scan rate of 10 mV s^{-1} after both activation steps (Figure 5a). The results of these investigations are summarized in Table S2. To obtain a current density of 5 mA cm^{-2} after Act_1, for all MnO_x an overpotential of 540 mV is needed. The OER onset potential (estimated at a current density of 0.1 mA cm^{-2}) is approximately 1.64 V *vs.* RHE for Mn^{II} and around 40 mV lower for Mn^{IV}. The performance of all samples improves during Act_2, revealing reduced overpotential values at 5 mA cm^{-2} and lower OER onset potentials, enhancing especially the catalytic activity of Mn^{II}, observed as a decreased overpotential by −110 mV. This is also noted in the Tafel slopes (Figure 5b), which decrease considerably by −35 mV dec^{-1} for Mn^{II} after Act_2. A more in-depth study of the activation procedures was carried out by comparing the degradation of current density as a function of the number of cycles for the 1st and the 2nd activation (Figure 6 and Figure S7). For Mn^{II} and Mn^{III}, no finite current value is

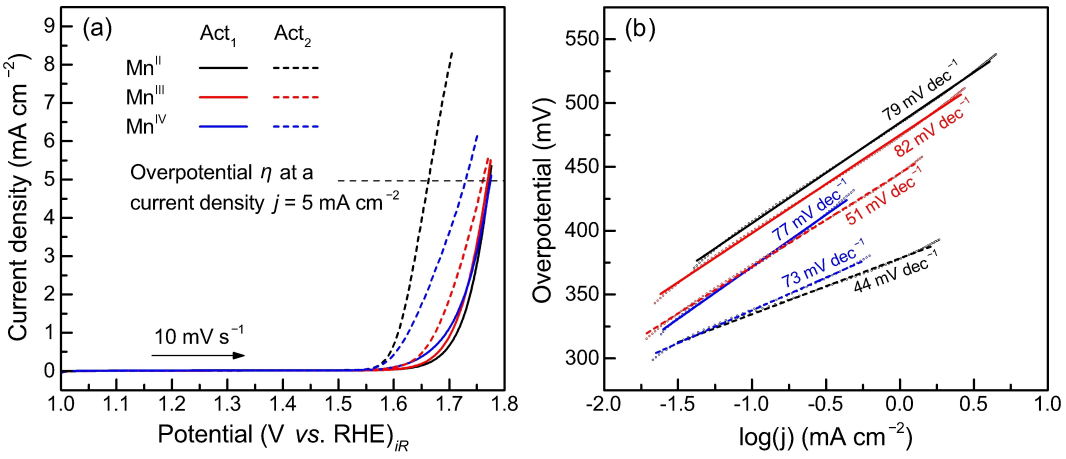

Figure 5. Activity comparison of MnO_x in 0.1 M KOH after the 1st activation (Act_1) and the 2nd activation (Act_2) steps. (a) Linear sweep voltammetry was used to determine the OER and the overpotential at 5 mA cm^{-2}, and (b) Tafel plots with linear fits to determine the Tafel slope.

observed after 20 cycles, although the changes in Mn^{III} are minimal throughout Act_1. The behavior of MnO_x changes after Act_2, enhancing the activity of Mn^{IV} during the first four cycles and staying constant afterwards. Mn^{II} and Mn^{III} behave inconsistent up to the latter cycles, suggesting ongoing oxidation. The activation process is associated with the oxidation of lower valent MnO_x species towards $Mn^{III,IV}$, in accordance with the early steady state reached of Mn^{IV} after only three activation cycles.[29,30]

Mn^{II} and Mn^{IV}, because of their change in activity, have been investigated further by XPS after both activation procedures (see Figure S8 for the survey spectra and Figure 7 for the relevant detail spectra). Additional XP peaks besides manganese and oxygen in the survey spectra are assigned to potassium (K 2p), originating from the used KOH electrolyte, and organic carbon. The Mn 2p region is used similarly as before to determine the main oxidation state of the MnO_x samples, as it is shown in Figure 7(a) and (c). $\Delta E2p_{1/2}$ values of 11.2 eV (Mn^{II}) and 11.4 eV (Mn^{IV}) have been identified after Act_1, and 11.6 eV after Act_2 for both samples. Concerning the previously stated $\Delta E2p_{1/2}$ of as-deposited MnO_2 (11.8 eV), the cycled samples are suspected to contain mostly Mn^{IV} with fractions of lower oxidized manganese, also due to the hydroxides (such as Mn^{II} in $Mn(OH)_2$ or Mn^{III} in MnOOH) identified in the O 1s region (Figure 7(b) and (d)). The lattice oxygen peak positions shift from 529.0 to 529.4 eV for the Mn^{IV} compound and from 530.2

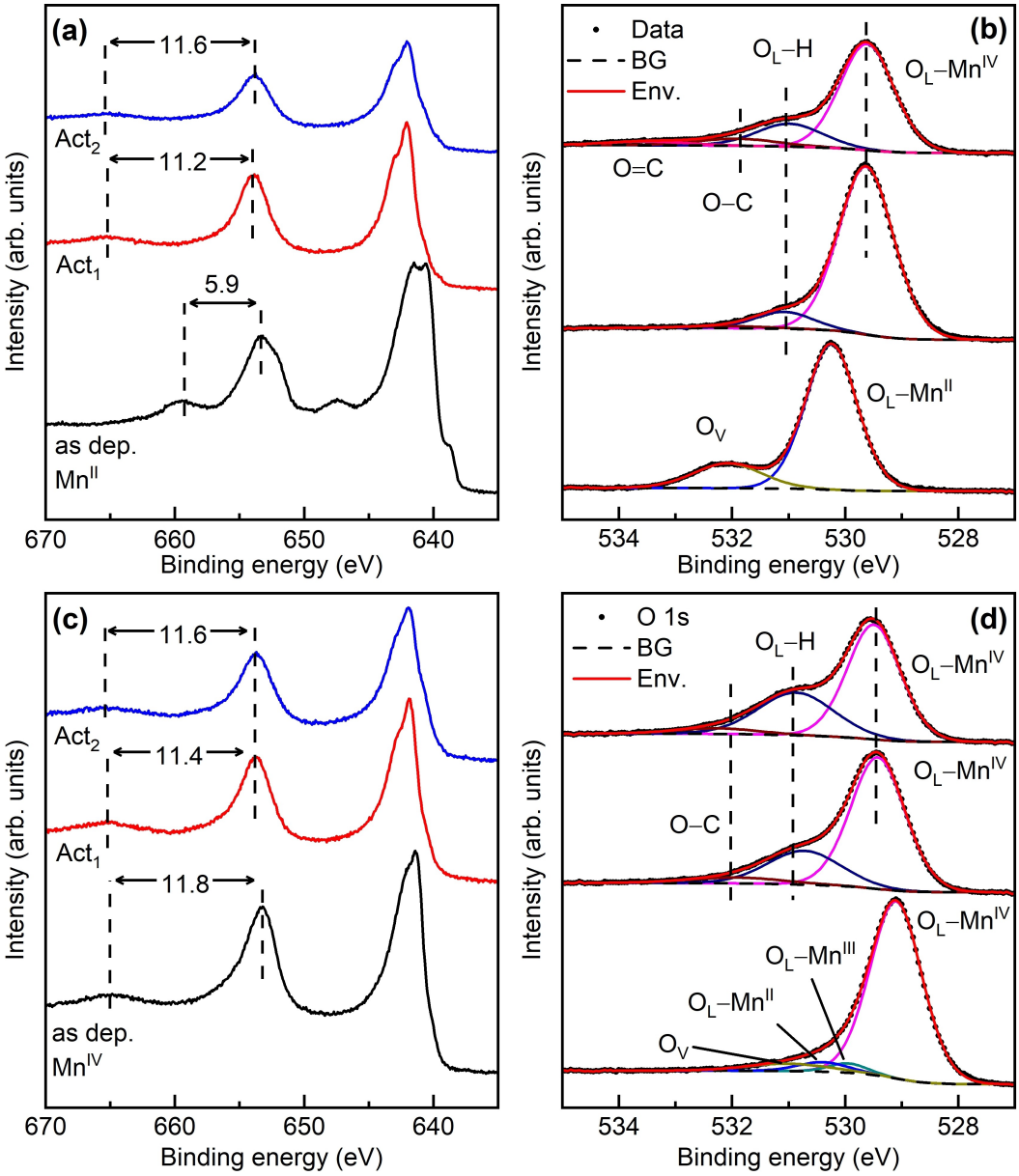

Figure 7. X-Ray photoelectron detail spectra of the freshly deposited, activated (Act_1), and reactivated (Act_2) (a,b) Mn^{II} and (c,d) Mn^{IV}. In the Mn 2p region, the distance between the $2p_{1/2}$ peak and $2p_{1/2}$ satellite is indicated. The O 1s region displays the lattice oxygen (O_L), oxygen induced vacancies (O_V), lattice hydroxides, and organic oxygen.

to 529.6 eV for the Mn^{II} sample. Both final peak positions are close to where the O_L–Mn^{III} was located before (529.7–529.9 eV, see Figure 1). Following the *operando* Raman results, cycling/activation of MnO_x creates Mn^{III} species, which can be detected by XPS, and are found to a greater extent in the treated Mn^{II}. Over cycling/activation, the amount of lattice hydroxide (O_L–H), which is located at 530.7–531.1 eV with FWHM values of 1.2–1.6 eV, increases with the number of cycles from 9.5–18.6% in Mn^{II} and 24.2–32.9% in Mn^{IV}.[73] Additionally, after electrochemistry, the samples contain organic carbon compounds such as O–C and O=C at 531.9–533.5 eV with a broader FWHM of 1.7–1.9 eV.[74]

SERS was also performed on the samples after both activation steps with the same parameters as for the freshly prepared films (see Figure 8). All spectra reveal the previously described three overlapping marker modes of Mn–O vibrations in $Mn^{IV}O_2$, along with a ν(O–O) band above 900 cm^{-1} for Mn^{II} after Act_1, which cannot be assigned precisely. Studies of single-crystalline Manganosite have assigned this signal to the TO + LO mode of $Mn^{II}O$.[75] It also might arise from MnO_4^- clusters because of residual potassium between MnO_x layers. We conclude that the most intense peak in the spectra consists of the overlapping $A_g(1)$ mode below 590 cm^{-1} and the $A_g(2)$ mode above 610 cm^{-1}. By analyzing the resulting peak position, the relative intensity of these bands is estimated. In Mn^{II} a blue-shift of the peak is visible from 587 to 599 cm^{-1}. An increase of the relative intensity of the $A_g(2)$ mode is estimated by the shift of the second out of plane stretching vibration from approximately 460 to 490 cm^{-1}. The resulting peak in Mn^{IV} red-shifts from 637 to 597 cm^{-1} while the second out of plane mode remains constant at around 485 cm^{-1}.

A well-defined assignment of the observed peak structure is not possible for the obtained Raman data. Directly after sample preparation, we did observe that our synthesis scheme most probably leads to a mixture of different MnO_x phases. This is also most likely the case for our sample after the electrochemical treatments. But the final shape of the spectra most closely resembles that what would be expected for a mixture of mainly Mn^{IV} oxidized species with a smaller amount of Mn^{III}. This interpretation, that the most active phase is a mixture of Mn^{III}, Mn^{IV} containing compounds is also well supported by our XPS data. Our interpretation is also in good agreement with previous investigations of MnO_x catalysts prepared by electrochemistry and characterized by various methods.[41,54] There the highest observed catalytic activity is attributed to a thin film containing mainly the mixed $Mn^{III,IV}$ oxide phases. They also observe the importance of potassium intercalation to form Birnessite-type layered structures, which is also observed in our XPS and *operando* Raman studies (see Figure 4 and S4).

3. Conclusion

Thin MnO_x films of approximately 10 nm in three different oxidation states (Mn^{II}, Mn^{III}, and Mn^{IV}) were deposited on electrochemically roughened gold substrates by reactive magnetron sputtering. With a combination of X-ray photoelectron and Raman spectroscopies, the chemical composition and structure of the samples was investigated. Their electrochemical performance was tested in 0.1 M KOH, in which the native Mn^{IV} oxide revealed the highest catalytic activity. By *operando* Raman spectroscopy we did observe, that in all samples a phase transformation towards Birnessite-type $Mn^{IV}O_2$ with increasing potential took place, differing for the diverse starting materials based on the Raman shift of two marker modes, which indicated the formation of Mn^{III} species, and the expansion of the interlayer distance between layers of MnO_6 octahedra. Furthermore, the widening of channels and layers is suggested by the incorporation of K^+ ions into the lattice, as it was observed from the MnO_4^- vibrational band in the *operando*

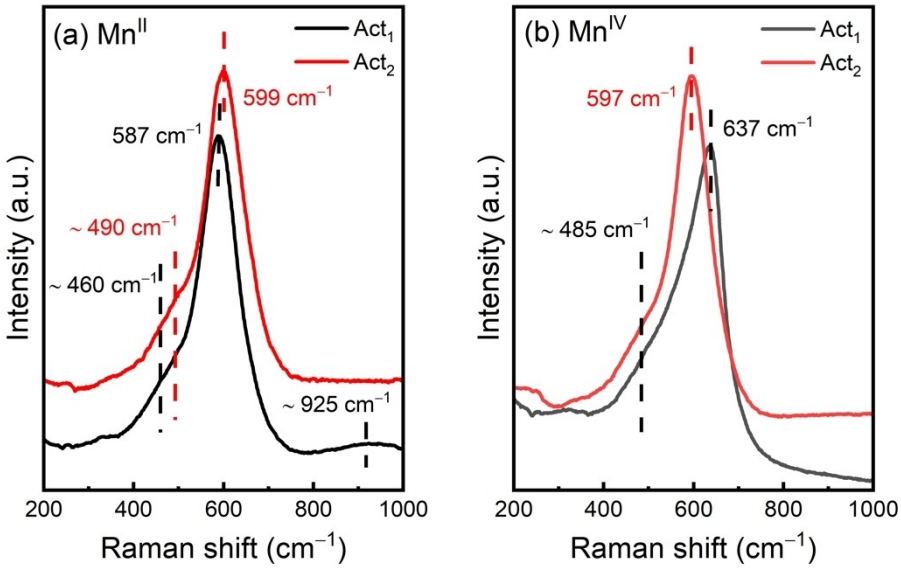

Figure 8. Surface enhanced Raman spectra of activated (Act_1) and reactivated (Act_2) (a) Mn^{II} and (b) Mn^{IV}.

Raman spectra at about 875 cm^{-1}, and by a residual K 2p signal in XPS after electrochemistry.

The catalytic activity towards the OER was greatly enhanced by an electrochemical activation treatment. After repeating the activation treatment once, no clear difference between Mn^{II} and Mn^{IV} was observed from the Raman spectra, indicating the formation of a similar structure motif. We conclude, that a $Mn^{III,IV}O_x$ is created during activation that is different from the originally deposited Mn^{II} and Mn^{IV}. From the broad features observed in the *operando* Raman and Raman spectra after activation we conclude that a highly amorphous mixed valence oxide has been formed during activation, which also leads to the material with the highest OER catalytic activity.

In summary, it must be noted that it is necessary to achieve a better understanding of MnO_x as OER catalyst, one must start with well-defined systems. This will hopefully lead to a better assignment of peak structures to the different phases. Also, further surface sensitive techniques will have to be employed, since the MnO_x seems to be one of the most complex systems with a large number of different phase compositions as well as the strong influence of the secondary structure on activity, conductivity, and surface area. Additionally, it is already clear from our experiments, that bulk, as well as surface changes, must be considered for the evaluation of the catalytic activity. Nevertheless, there are quite some similarities between our inorganic catalyst and the active complex in PS II. Both show a low efficiency (solar to fuel for PS II and a high overpotential and low stability for our films), the secondary structure plays an important role for the different oxidation steps, and both require additional alkaline or alkaline earth metals during oxygen evolution.

Acknowledgments

This work was financially supported by the German Federal Ministry of Education and Research (BMBF cluster project MANGAN FKZ 03S0506). H.R, W.J. and B.K. are members of the Graduate School of Excellence by the German Science Foundation (DFG GSC 1070) "Energy Science and Engineering". B.K. and W.J. acknowledge partial financial support by the Deutsche Forschungsgemeinschaft (DFG JA 859/34-1). The authors thank Lukas Stühn for conducting the AFM measurement and the group of Professor Ralf Riedel for their support in Raman spectroscopy. Open access funding enabled and organized by Projekt DEAL.

Conflict of Interest

The authors declare no conflict of interest.

Keywords: *operando* Raman spectroscopy · X-ray photoelectron spectroscopy · manganese oxide · oxygen evolution reaction · electrocatalysis

[1] M. Höök, X. Tang, *Energy Policy* **2013**, *52*, 797.
[2] A. Stips, D. Macias, C. Coughlan, E. Garcia-Gorriz, X. S. Liang, *Sci. Rep.* **2016**, *6*, 21691.
[3] H. B. Gray, *Nat. Chem.* **2009**, *1*, 7.
[4] W. A. Braff, J. M. Mueller, J. E. Trancik, *Nat. Clim. Change* **2016**, *6*, 964.
[5] S. Chu, Y. Cui, N. Liu, *Nat. Mater.* **2016**, *16*, 16.
[6] S. Dunn, *Int. J. Hydrogen Energy* **2002**, *27*, 235.
[7] A. Zuttel, A. Remhof, A. Borgschulte, O. Friedrichs, *Philos. Trans. R. Soc. London Ser. A* **2010**, *368*, 3329.
[8] I. Dincer, C. Acar, *Int. J. Hydrogen Energy* **2018**, *43*, 8579.
[9] Y. Jiao, Y. Zheng, M. Jaroniec, S. Z. Qiao, *Chem. Soc. Rev.* **2015**, *44*, 2060.
[10] Y. Lee, J. Suntivich, K. J. May, E. E. Perry, Y. Shao-Horn, *J. Phys. Chem. Lett.* **2012**, *3*, 399.
[11] B. Su, Z. C. Cao, Z. J. Shi, *Acc. Chem. Res.* **2015**, *48*, 886.
[12] M. M. Najafpour, S. I. Allakhverdiev, *Int. J. Hydrogen Energy* **2012**, *37*, 8753.
[13] M. Yagi, M. Kaneko, *Chem. Rev.* **2001**, *101*, 21.
[14] S. Cherevko, S. Geiger, O. Kasian, N. Kulyk, J.-P. Grote, A. Savan, B. R. Shrestha, S. Merzlikin, B. Breitbach, A. Ludwig, K. J. J. Mayrhofer, *Catal. Today* **2016**, *262*, 170.
[15] C. Hu, L. Zhang, J. Gong, *Energy Environ. Sci.* **2019**, *12*, 2620.
[16] A. Pichon, *Nat. Chem.* **2015**, *7*, 465.
[17] S. Geller, *Acta Crystallogr. Sect. B* **1971**, *27*, 821.
[18] A. Yamaguchi, R. Inuzuka, T. Takashima, T. Hayashi, K. Hashimoto, R. Nakamura, *Nat. Commun.* **2014**, *5*, 4256.
[19] C. M. Julien, M. Massot, C. Poinsignon, *Spectrochim. Acta Part A* **2004**, *60*, 689.
[20] B. Lee, C. S. Yoon, H. R. Lee, K. Y. Chung, B. W. Cho, S. H. Oh, *Sci. Rep.* **2014**, *4*, 6066.
[21] B. R. Chen, W. Sun, D. A. Kitchaev, J. S. Mangum, V. Thampy, L. M. Garten, D. S. Ginley, B. P. Gorman, K. H. Stone, G. Ceder, M. F. Toney, L. T. Schelhas, *Nat. Commun.* **2018**, *9*, 2553.
[22] C. Julien, *Solid State Ionics* **2003**, *159*, 345.
[23] B. M. Weckhuysen, *Chem. Commun.* **2002**, *2*, 97.
[24] Z. W. Seh, J. Kibsgaard, C. F. Dickens, I. Chorkendorff, J. K. Nørskov, T. F. Jaramillo, *Science* **2017**, *355*.
[25] B. M. Hunter, H. B. Gray, A. M. Müller, *Chem. Rev.* **2016**, *116*, 14120.
[26] M. O. Guerrero-Pérez, M. A. Bañares, *Catal. Today* **2006**, *113*, 48.
[27] I. E. Wachs, C. A. Roberts, *Chem. Soc. Rev.* **2010**, *39*, 5002.
[28] M. A. Bañares, M. O. Guerrero-Pérez, J. L. G. Fierro, G. G. Cortez, *J. Mater. Chem.* **2002**, *12*, 3337.
[29] M. C. Bernard, *J. Electrochem. Soc.* **1993**, *140*, 3065.
[30] B. Messaoudi, S. Joiret, M. Keddam, H. Takenouti, *Electrochim. Acta* **2001**, *46*, 2487.
[31] M. Rabe, C. Toparli, Y.-H. Chen, O. Kasian, K. J. J. Mayrhofer, A. Erbe, *Phys. Chem. Chem. Phys.* **2019**, *21*, 10457.
[32] D. Gosztola, M. J. Weaver, *J. Electroanal. Chem.* **1989**, *271*, 141.
[33] G. M. Herrera, A. C. Padilla, S. P. Hernandez-Rivera, *Nanomaterials* **2013**, *3*, 158.
[34] L. Zhong, D. Chen, S. Zafeiratos, *Catal. Sci. Technol.* **2019**, *9*, 3851.
[35] E. S. Ilton, J. E. Post, P. J. Heaney, F. T. Ling, S. N. Kerisit, *Appl. Surf. Sci.* **2016**, *366*, 475.
[36] N. J. Dou, Z. Sun, A. Opalade, N. Wang, W. Fu, F. F. Tao, *Chem. Soc. Rev.* **2017**, *46*, 2001.
[37] O. Diaz-Morales, D. Ferrus-Suspedra, M. T. M. Koper, *Chem. Sci.* **2016**, *7*, 2639.
[38] T. Gao, H. Fjellvåg, P. Norby, *Anal. Chim. Acta* **2009**, *648*, 235.
[39] J. F. Moulder, J. Chastain, *Handbook of x-ray photoelectron spectroscopy*, Physical Electronics, Minnesota, **1995**.
[40] M. A. Stranick, *Surf. Sci. Spectra* **1999**, *6*, 31.
[41] Y. Gorlin, T. F. Jaramillo, *J. Am. Chem. Soc.* **2010**, *132*, 13612.
[42] Y. Gorlin, B. Lassalle-Kaiser, J. D. Benck, S. Gul, S. M. Webb, V. K. Yachandra, J. Yano, T. F. Jaramillo, *J. Am. Chem. Soc.* **2013**, *135*, 8525.
[43] V. Di Castro, G. Polzonetti, *J. Electron Spectrosc. Relat. Phenom.* **1989**, *48*, 117.
[44] M. A. Stranick, *Surf. Sci. Spectra* **1999**, *6*, 39.
[45] M. C. Biesinger, B. P. Payne, A. P. Grosvenor, L. W. M. Lau, A. R. Gerson, R. S. C. Smart, *Appl. Surf. Sci.* **2011**, *257*, 2717.
[46] N. Zhang, L. Li, Y. Chu, L. Zheng, S. Sun, G. Zhang, H. He, J. Zhao, *Catal. Today* **2019**, *332*, 101.
[47] S. Jain, J. Shah, N. S. Negi, C. Sharma, R. K. Kotnala, *Int. J. Energy Res.* **2019**, *43*, 4743.
[48] J. E. Post, *Proc. Mont. Acad. Sci.* **1999**, *96*, 3447.
[49] F. Wang, H. Dai, J. Deng, G. Bai, K. Ji, Y. Liu, *Environ. Sci. Technol.* **2012**, *46*, 4034.

[50] C. Ji, H. Ren, S. Yang, *RSC Adv.* **2015**, *5*, 21978.
[51] I. G. McKendry, S. K. Kondaveeti, S. L. Shumlas, D. R. Strongin, M. J. Zdilla, *Dalton Trans.* **2015**, *44*, 12981.
[52] S. Bernardini, F. Bellatreccia, G. Della Ventura, P. Ballirano, A. Sodo, *RSC Adv.* **2020**, *10*, 923.
[53] T. Gao, H. Fjellvåg, P. Norby, *Anal. Chim. Acta* **2009**, *648*, 235.
[54] E. Widjaja, J. T. Sampanthar, *Anal. Chim. Acta* **2007**, *585*, 241.
[55] S. Bernardini, F. Bellatreccia, A. Casanova Municchia, G. Della Ventura, A. Sodo, *J. Raman Spectrosc.* **2019**, *96*, 3447.
[56] H. An, Z. Chen, J. Yang, Z. Feng, X. Wang, F. Fan, C. Li, *J. Catal.* **2018**, *367*, 53.
[57] C. Julien, M. Massot, S. Rangan, M. Lemal, D. Guyomard, *J. Raman Spectrosc.* **2002**, *33*, 223.
[58] C. Burlet, Y. Vanbrabant, *J. Raman Spectrosc.* **2015**, *46*, 941.
[59] F. Wan, H. Shi, W. Chen, Z. Gu, L. Du, P. Wang, J. Wang, Y. Huang, *Nanomaterials* **2017**, *7*, 210.
[60] M. Rycenga, M. H. Kim, P. H. C. Camargo, C. Cobley, Z.-Y. Li, Y. Xia, *J. Phys. Chem. A* **2009**, *113*, 3932.
[61] F. Buciuman, F. Patcas, R. Craciun, D. R. T. Zahn, *Phys. Chem. Chem. Phys.* **1999**, *1*, 185.
[62] N. Mironova-Ulmane, A. Kuzmin, V. Skvortsova, G. Chikvaidze, I. Sildos, J. Grabis, D. Jankoviča, A. Dindune, M. Maiorov, *Acta Phys. Pol. A* **2018**, *133*, 1013.
[63] Z. M. Chan, Z. Morgan, D. A. Kitchaev, J. N. Weker, C. Schnedermann, K. Lim, G. Ceder, W. Tumas, M. F. Toney, D. G. Nocera, *Proc. Natl. Acad. Sci. U. S. A.* **2018**, *115*, 5261.
[64] A. Byström, A. M. Byström, *Acta Crystallogr.* **1950**, *3*, 146.
[65] A. Manceau, V. A. Drits, E. Silvester, C. Bartoli, B. Lanson, *Am. Mineral.* **1997**, *82*, 1150.
[66] M. Pourbaix, *Atlas of electrochemical equilibria in aqueous solutions.* Houston, Texas, **1974**.
[67] M. Risch, K. A. Stoerzinger, B. Han, T. Z. Regier, D. Peak, S. Y. Sayed, C. Wei, Z. Xu, Y. Shao-Horn, *J. Phys. Chem C* **2017**, *121*, 17682.
[68] M. Fekete, R. K. Hocking, S. L. Y. Chang, C. Italiano, A. F. Patti, F. Arena, L. Spiccia, *Energy Environ. Sci.* **2013**, *6*, 2222.
[69] P. Connor, J. Schuch, B. Kaiser, W. Jaegermann, *Z. Phys. Chem.* **2020**, *234*, 979.
[70] R. K. Khanna, D. D. Stranz, *Spectrochim. Acta Part A* **1980**, *36*, 387.
[71] C. Engert, W. Kiefer, *J. Raman Spectrosc.* **1991**, *22*, 715.
[72] W. Kiefer, H. J. Bernstein, *Appl. Spectrosc.* **1971**, *25*, 609.
[73] H. R. Barai, A. N. Banerjee, S. W. Joo, *J. Ind. Eng. Chem.* **2017**, *56*, 212.
[74] G. Greczynski, L. Hultman, *ChemPhysChem* **2017**, *18*, 1507.
[75] N. Mironova-Ulmane, A. Kuzmin, M. Grube, *J. Alloys Compd.* **2009**, *480*, 97.

Manuscript received: October 27, 2020
Revised manuscript received: November 24, 2020
Accepted manuscript online: November 24, 2020
Version of record online: December 16, 2020